applied sciences

MDPI

Article

Photocatalytic Degradation of Methylene Blue Dye by Electrospun Binary and Ternary Zinc and Titanium Oxide Nanofibers

Beatrix Petrovičová [1], Zainab Dahrouch [2], Claudia Triolo [1], Fabiola Pantò [3], Angela Malara [1], Salvatore Patanè [4,*], Maria Allegrini [5] and Saveria Santangelo [1,*]

[1] Dipartimento di Ingegneria Civile, dell'Energia, dell'Ambiente e dei Materiali (DICEAM), Università "Mediterranea", 89122 Reggio Calabria, Italy; beatrix.petrovicova@unirc.it (B.P.); claudia.triolo@unirc.it (C.T.); angela.malara@unirc.it (A.M.)

[2] Laboratoire Physico-Chimie des Matériaux, Substances Naturelles et Environnement, Département de Génie Chimique, Faculté des Sciences et Techniques de Tanger, Ancienne Route de l'Aéroport, Km 10, Ziaten, BP 416, Tanger 90000, Morocco; zainabdahrouch@gmail.com

[3] Istituto di Tecnologie Avanzate per l'Energia (ITAE) del Consiglio Nazionale delle Ricerche (CNR), 98126 Messina, Italy; fabiola.panto@itae.cnr.it

[4] Dipartimento di Scienze Matematiche e Informatiche, Scienze Fisiche e Scienze della Terra (MIFT), Università di Messina, 98166 Messina, Italy

[5] Istituto Nanoscienze-CNR, Dipartimento di Fisica "E. Fermi", Università di Pisa, Largo Bruno Pontecorvo 3, 56127 Pisa, Italy; maria.allegrini@unipi.it

* Correspondence: patanes@unime.it (S.P.); saveria.santangelo@unirc.it (S.S.)

Citation: Petrovičová, B.; Dahrouch, Z.; Triolo, C.; Pantò, F.; Malara, A.; Patanè, S.; Allegrini, M.; Santangelo, S. Photocatalytic Degradation of Methylene Blue Dye by Electrospun Binary and Ternary Zinc and Titanium Oxide Nanofibers. *Appl. Sci.* **2021**, *11*, 9720. https://doi.org/10.3390/app11209720

Academic Editors: Nhamo Chaukura, Alex Kuvarega and Rangabhashiyam Selvasembian

Received: 5 October 2021
Accepted: 14 October 2021
Published: 18 October 2021

Abstract: Synthetic dyes, dispersed in water, have harmful effects on human health and the environment. In this work, Ti and/or Zn oxide nanofibers (NFs) with engineered architecture and surface were produced via electrospinning followed by calcination. Calcination and subsequent cooling were operated at fast rates to generate porous NFs with capture centers to reduce the recombination rate of the photogenerated charges. After morphological and microstructural characterisation, the NFs were comparatively evaluated as photocatalysts for the removal of methylene blue from water under UV irradiation. The higher band gap and lower crystallinity were responsible for the lower photocatalytic activity of the ternary oxides ($ZnTiO_3$ and Zn_2TiO_4) towards the degradation of the dye. The optimal loads of the highly performing binary oxides were determined. By using 0.66 mg mL^{-1} wurtzite ZnO for the discoloration of an aqueous solution with a dye concentration of 15 μM, a higher rate constant (7.94×10^{-2} min^{-1}) than previously reported was obtained. The optimal load for anatase TiO_2 was lower (0.33 mg mL^{-1}). The corresponding rate constant (1.12×10^{-1} min^{-1}) exceeds the values reported for the commonly used P25–TiO_2 benchmark. The catalyst can be reused twice without any regeneration treatment, with 5.2% and 18.7% activity decrease after the second and third use, respectively.

Keywords: methylene blue dye; photodegradation; nanofibers; capture centers; anatase; zinc oxide

1. Introduction

"Clean water and sanitation" represent the sixth of the seventeen sustainable development goals (SDGs) unanimously adopted by the 193 members of the United Nations General Assembly in 2015 [1]. The increase in the world population, together with the effects of climate change, is making the availability of drinking water insufficient to meet the ever-increasing demand. The increase in the level of water pollution due to anthropogenic factors also contributes to this phenomenon.

Due to their toxic and non-biodegradable nature, synthetic dyes, massively used in the textile industry for dyeing fabrics, represent a serious danger for the environment. In

the absence of proper management, the discharge of textile wastewater into the surrounding environment, as often happens in developing countries, is a source of severe damage to the environment and constitutes a serious risk to human health [2,3]. Dispersed in water, the dyes inhibit the transmission of light, which causes a reduction in the dissolved oxygen levels and rate of photosynthesis [4]; their ingestion has harmful effects such as gastrointestinal and urogenital diseases, irritation of the mucous membranes, dermatology, and alterations of the blood [5]. 3,7-Bis(dimethylamino)-phenothiazin-5-ium chloride, better known as methylene blue (MB), is a broadly utilized dye in the textile industry [6]. Its use is also extended to the pharmaceutical, printing, cosmetics, leather, and food industries [7]. The presence of aromatic rings in its structure makes difficult its complete removal [8].

In the last decades, advanced oxidation processes, including both homogenous and heterogeneous catalysis, have been frequently employed to remove a wide range of inorganic and organic contaminants from water and wastewater [9–11]. Various semiconducting metal oxides have been successfully utilized as heterogeneous catalysts for the photo-assisted degradation of dye pollutants [12–19]. Among them, zinc oxide (ZnO) [20–22] and titanium dioxide (TiO_2) [3,23,24] have received particular attention thanks to their non-toxicity, chemical stability, biocompatibility, and low-cost.

Recently, the use of coupled ZnO–TiO_2 photocatalysts has been proposed for MB degradation under ultraviolet (UV) or visible (VIS) light irradiation [25–31]. Chen et al. [30] have followed the hydrothermal route to prepare coupled ZnO–TiO_2 nanocomposites consisting of ZnO nanorods (NRs) decorated by TiO_2 nanoparticles (NPs). They show that, thanks to the favorable electron-transfer properties of the heterojunctions ZnO/TiO_2, the coupled ZnO–TiO_2 nanocomposites exhibit largely improved degradation performance with respect to both ZnO NRs and TiO_2 NPs. Singh et al. [29] have produced ZnO–TiO_2 nanohybrids for sunlight-driven photodegradation of textile dyes and other pollutant molecules via the hydrothermal method. The superior photodegradation performance of the nanohybrids, consisting of ZnO nanoflakes functionalized with TiO_2 nanoparticles with one- (1D) or three-dimensional (3D) architecture depending on the Zn:Ti volume ratio, is attributed to the ZnO/TiO_2 synergy induced increased charge separation efficiency. Someswararao et al. [28] have reported about electrospun ZnO/TiO_2 composites nanofibers (NFs) endowed with enhanced photocatalytic activity with respect to both single-metal oxide NFs. Liu et al. [31] have synthesized coaxial ZnO/TiO_2 core/shell NFs needing less energy to be activated and showing better photocatalytic activity for the degradation of MB than ZnO, TiO_2 or blending ZnO–TiO_2 NFs. Lee et al. [26] have prepared composite Ti/Zn-based NFs, containing ZnO, TiO_2, Ti_2O_3, and $ZnTiO_3$ oxides, with improved photocatalytic performance compared to TiO_2.

Upon irradiation with photons having sufficient energy, electrons (e^-) on the surface of the photocatalyst are excited to the conduction band (CB) and holes (h^+) are generated in the valence band (VB). The e^--h^+ pairs can either recombine and produce thermal energy or react with adsorbed water, oxygen, and organic species via oxidation and reduction reactions [21,23,32–34]. As sketched in Figure S1, the trapping of e^- by oxygen molecules gives rise to superoxide radicals ($O_2^{\bullet}$); the reaction of h^+ with the chemisorbed water molecules leads to the formation of hydroxyl groups (OH^-) or hydroxyl radicals ($OH^{\bullet}$) and maintains electrical neutrality within the catalyst [23,32]. The dye degradation and complete oxidation in non-toxic organic products can occur through (*i*) direct and (*ii*) indirect oxidation via the reaction with h^+ and $OH^{\bullet}$ radicals, respectively [32,33,35].

Lattice defects (such as vacancies and/or interstitials) that introduce trap states in the band gap [36] strongly affect the recombination rate of the photogenerated e^--h^+ pairs and, hence, the catalyst activity toward the dye molecule degradation [20,21]. Introducing e^--capture centers, through doping [34] or surface engineering [20,21], to reduce the probability of the e^--h^+ recombination, has been shown to be a viable strategy to enhance the photocatalytic efficiency of ZnO. Moreover, morphology and specific surface area have a great influence [20].

Electrospinning (ES) is a simple and cost-effective technique widely utilized for the growth of high aspect-ratio and surface-area (organic, inorganic, and hybrid) nanostructures with different morphologies [37–39] used in a great variety of applications ranging from energy conversion and storage, to biomedicine, gas sensing, and water remediation [37,40–43]. ES scalability and the availability of commercial machineries capable of producing fibrous sheets of up to 300–600 m^2 in size make it a suitable technique for the production of NF catalysts on an industrial scale.

This work deals with binary (Ti or Zn) or ternary (Ti and Zn) oxide NFs and the comparative evaluation of their photocatalytic activity towards the degradation of MB in an aqueous solution. In order to produce porous NFs and generate capture centers located at the boundaries between the oxide grains constituting them, calcination and subsequent cooling were operated at fast rates. The critical features of the produced NFs were investigated to find out if the conclusions previously drawn on the key role of defects in the design of ZnO photocatalyst have more general validity. The optimal loads of the best performing NFs were determined to maximize the efficiency of the photocatalytic process, which is a fundamental recipe for its industrial use. Moreover, the photocatalyst reusability was investigated.

2. Experimental Section

2.1. Reagents and Chemicals

For the preparation of the precursor solutions, we use as-received titanium (IV)butoxide, $Ti(OCH_2CH_2CH_2CH_3)_4$ (purity: 97%; CAS No. 5593-70-4, Sigma Aldrich, Burlington, MA, USA), zinc acetate dehydrate, $Zn(CH_3COO)_2{\cdot}2H_2O$ (purity: 98%; CAS No. 5970-45-6, Fischer Scientific, Hampton, NH, USA), polyacrylonitrile, $(C_3H_3N)_n$ (average molecular weight: 150,000 g mol^{-1}; purity: 99.9%; CAS No. 25014-41-9, Sigma Aldrich), and *N*,*N*-dimethylformamide, $HCON(CH_3)_2$ (anhydrous: 99.8%; CAS No. 68-12-2, Sigma Aldrich). Titanium butoxide (TiBO) and zinc acetate ($ZnAc_2$) acted as Ti and Zn sources, respectively; polyacrylonitrile (PAN) and *N*,*N*-dimethylformamide (DMF) were used as polymer and solvent, respectively. Sodium hydroxide, NaOH (purity: 98%; CAS No. 1310-73-10, Sigma Aldrich), was used for the post-growth chemical treatment. The MB dye $C_{16}H_{18}ClN_3S$ (purity: 99%; CAS 61-73-4) was from Sigma Aldrich.

2.2. Synthesis of the Photocatalysts

We have prepared the photocatalysts via ES by following the experimental procedure illustrated below. First, the precursor solution was prepared by the sol–gel method. Typically, 0.325 g PAN was dissolved in 4.550 g DMF and the resulting solution was stirred until it became clear. Subsequently, stoichiometric amounts of TiBO and/or $ZnAc_2$ were added (Table 1), and the solution was magnetically stirred for 2 h at room temperature (RT). The as-obtained homogeneous solution was electrospun at 20 ± 1 °C (relative air humidity: 40%) via a CH-01 Electro-spinner 2.0 (Linari Engineering s.r.l.). The solution, loaded in a 20 mL syringe equipped with a 40 mm long 0.8 mm gauge stainless steel needle, was fed at a rate of 23.5 μL min^{-1}. A 17 kV DC voltage was applied over a collection distance of 11 cm. The electrospun NFs were collected on a grounded aluminum foil. After drying at RT overnight to remove the DMF residuals, they were peeled from the collector and calcined in air to obtain the oxide from the precursor(s). Heating was carried at a fast rate (10 °C min^{-1}) to obtain mostly hollow NFs consisting of interconnected nanograins [44]. After 2 h at 600 °C, the crucible was picked up from the oven and immersed in an ice bath to fast cool the as-calcined sample and generating capture centers [21].

TiO_2 and ZnO are expected to form via the combustion reactions $Ti(OCH_2CH_2CH_2CH_3)_4 + 24\,O_2 \rightarrow TiO_2 + 18\,H_2O + 16\,CO_2$ and $Zn(CH_3COO)_2 + 4\,O_2 \rightarrow ZnO + 3\,H_2O + 4\,CO_2$, respectively. Further details on the photocatalyst preparation can be found in Reference [21]. The Ti- and/or Zn-based photocatalysts were coded as TZxy, with

xy standing for the Ti:Zn molar ratio; TZ10 and TZ01 denoted binary Ti and Zn-oxide photocatalysts, respectively.

In order to increase its surface area [45], sample TZ21 was chemically etched by immersion into a 2.5 M solution of NaOH. After 2 h stirring at RT, the sample was washed with de-ionized water several times and dried overnight at 80 °C. The so-obtained material was coded as TZ21NaOH.

Table 1. Codes of the samples and stoichiometric amounts of titanium butoxide (TiBO) and zinc acetate ($ZnAc_2$) utilized for their preparation. The phase(s) of the oxide formed is (are) also reported (with secondary phase in brackets).

Sample Code	TiBO/mmol	$ZnAc_2$/mmol	Resulting Phase(s)
TZ10	2.60	0.00	*a*-TiO_2
TZ21	1.73	0.87	$ZnTiO_3$ (*a*-TiO_2 + *r*-TiO_2)
TZ11	1.30	1.30	disordered Zn_2TiO_4 (*r*-TiO_2)
TZ12	0.87	1.73	Zn_2TiO_4 (*r*-TiO_2)
TZ01	0.00	2.60	ZnO

2.3. Characterization

After their preparation, we thoroughly analyzed these samples. Their texture and morphology were investigated by scanning electron microscopy (SEM) and atomic force microscopy (AFM). The crystalline phase of the oxide was identified by X-ray powder diffraction (XRPD), while its crystallinity degree was evaluated via micro-Raman spectroscopy (MRS). SEM images were recorded by a Phenom Pro-X scanning electron microscope equipped with an energy-dispersive X-ray (EDX) spectrometer. A NT-MDT Integra Spectra C microscope operating in intermittent contact mode was used to acquire the AFM images. The XRPD patterns were recorded at a scan speed of 0.5°/min by using the Ni β-filtered Cu-K_α radiation (λ = 0.15404 nm) at 40 kV. The diffraction peak identification was performed by utilizing the JCPDS database of reference compounds. Raman scattering excited by a solid-state laser operating at 532 nm (2.33 eV) was measured by means of a NTEGRA-Spectra SPM NT-MDT confocal microscope. To prevent local heating the laser power was set at 250 μW at the sample surface. The scattered light from the sample was collected by means of a 100× Mitutoyo objective and detected via a cooled ANDOR iDus CCD Camera. To evaluate the spatial homogeneity of the samples, spectra from several random locations on each specimen were recorded and subsequently averaged to have a reliable picture of the entire sample. Further details on the instrumentation can be found in References [21,46].

2.4. Evaluation of the Photocatalytic Activity and Assessment of the Optimal Load

Unless differently specified, the activity of the Ti- and/or Zn-based photocatalysts toward the removal of MB was evaluated under UV irradiation. A 350-nm (3.54 eV) lamp with a power density of 10 mW cm^{-2} acted as a radiation source. The as-supplied MB reagent grade was used as a dye. The desired amount of photocatalyst was dispersed in 3 mL of 15 μM MB solution. Before being exposed to the radiation, the solution was magnetically stirred in the dark for 1 h to achieve adsorption/desorption equilibrium between dye solution and photocatalyst. Then, it was centrifuged (1000 rpm, 2 min) to segregate the photocatalyst particles before performing the zero-time measurement. Subsequently, the suspension was exposed to the radiation, at given time intervals. At the end of each interval, the solution was centrifuged again, and its optical absorbance was measured to evaluate the MB concentration. A Perkin-Elmer Lambda 2 UV–Vis spectrophotometer was used for this purpose. Measurements were conducted also on 3 mL of 15 μM MB without the addition of any catalyst.

In order to investigate the effect of the photocatalyst concentration on the degradation efficiency, different amounts of the oxide NFs (0.3, 1.0, 2.0 and 3.0 mg, corresponding to loads of 0.10, 0.33, 0.66, and 1.00 mg mL^{-1}) were dispersed in the MB

solution. The reusability of the best performing photocatalyst was further evaluated, under optimal load conditions, without any separation or washing procedure with water.

3. Results and discussion

3.1. Morphological and Textural Properties of the Photocatalysts

Figures 1 and S2 display the results of the SEM/EDX analysis on the as-calcined photocatalysts. Although all the samples consist of NFs, the variation of the Ti:Zn molar ratio from 1:0 to 0:1 reflects on evident changes in the NF texture, morphology (Figure 1a–e), and diameters (Figure 1f). In sample TZ10, the fibers look relatively smooth and uniform in diameter along their axis; only a few beads are observed. On the contrary, in samples TZ21, TZ11, and TZ12, the NFs are beaded to larger extents. Sample TZ01 exhibits rough NFs, already described in detail in previous work [21]. The comparison with other electrospun Ti- and/or Zn-oxide NFs [26–28] evidences some morphological differences; they arise from the different preparation conditions selected. The NF diameter distributions, as measured by the image analysis software of the microscope, are shown in the insets of Figure 1a–e; the corresponding ranges of NF diameters and center values of the distributions are reported in Figure 1f. The center value of the distributions increases in the order TZ01 < TZ10 < TZ11 < TZ21 < TZ12.

The EDX analysis (Figure S2) confirms the inorganic nature of the NFs and the complete degradation of the organic constituents present before calcination; the elemental mapping proves the spatially uniform distribution of oxygen, titanium, and/or zinc throughout the NFs.

3.2. Crystalline Phase, Spatial Homogeneity, and Crystallinity Degree of the Oxide

The crystalline phase of the oxide formed upon calcination was assessed via the XRPD analysis (Figure 2a). The diffractogram of sample TZ10 exhibits the peaks typical of the anatase (*a*-TiO_2) tetragonal phase of titania (JCPDS Card No. 21-1272) [28,30,47]. The diffraction peaks of sample TZ01 can be indexed to reflections from the crystallographic planes of the wurtzite hexagonal structure of zincite phase (ZnO, JCPDS card No. 36-1451) [20,21,28,30,47]. The comparison with the literature [26–28] proves that the crystalline phase formed in the Ti- and Zn-oxide NFs strongly depends on the Ti:Zn molar ratio in the precursor solution. Most of the peaks appearing in the diffractogram of sample TZ21 are peculiar to the ilmenite-type zinc meta-titanate ($ZnTiO_3$) with hexagonal structure (JCPDS Card No. 26-1500) [48]; besides, two weaker peaks compatible with the formation of *a*-TiO_2 and rutile (*r*-TiO_2, JCPDS Card No. 21-1276) phases of titania are detected. Most of the diffraction peaks of sample TZ12 can be indexed to reflections from the crystallographic planes of the zinc ortho-titanate (Zn_2TiO_4) with inverse spinel structure (JCPDS Card No. 19-1483) [49,50]; in addition, some weak signal compatible with the presence of *r*-TiO_2 as a secondary phase is observed. In the diffractogram of sample TZ11, the peaks are substantially located at the same angular positions as in sample TZ12, but they are much broader, indicating lower crystallinity and/or crystal size. The average size of the oxide crystallites was estimated from the most intense peak of each XRPD pattern via the Scherrer's formula, $d_C = K\lambda/\beta\cos\theta$, where K (0.9) is the Scherrer constant, λ (0.1541 nm) stands for the X-ray wavelength, β indicates the FWHM (full width at half maximum) of the diffraction peak, and θ denotes the reflection angle [21,51]. The d_C values obtained (reported in Figure 2a) range between 6.5 and 27.6 nm; they increase in the order TZ11 < TZ12 < TZ21 < TZ01 < TZ10.

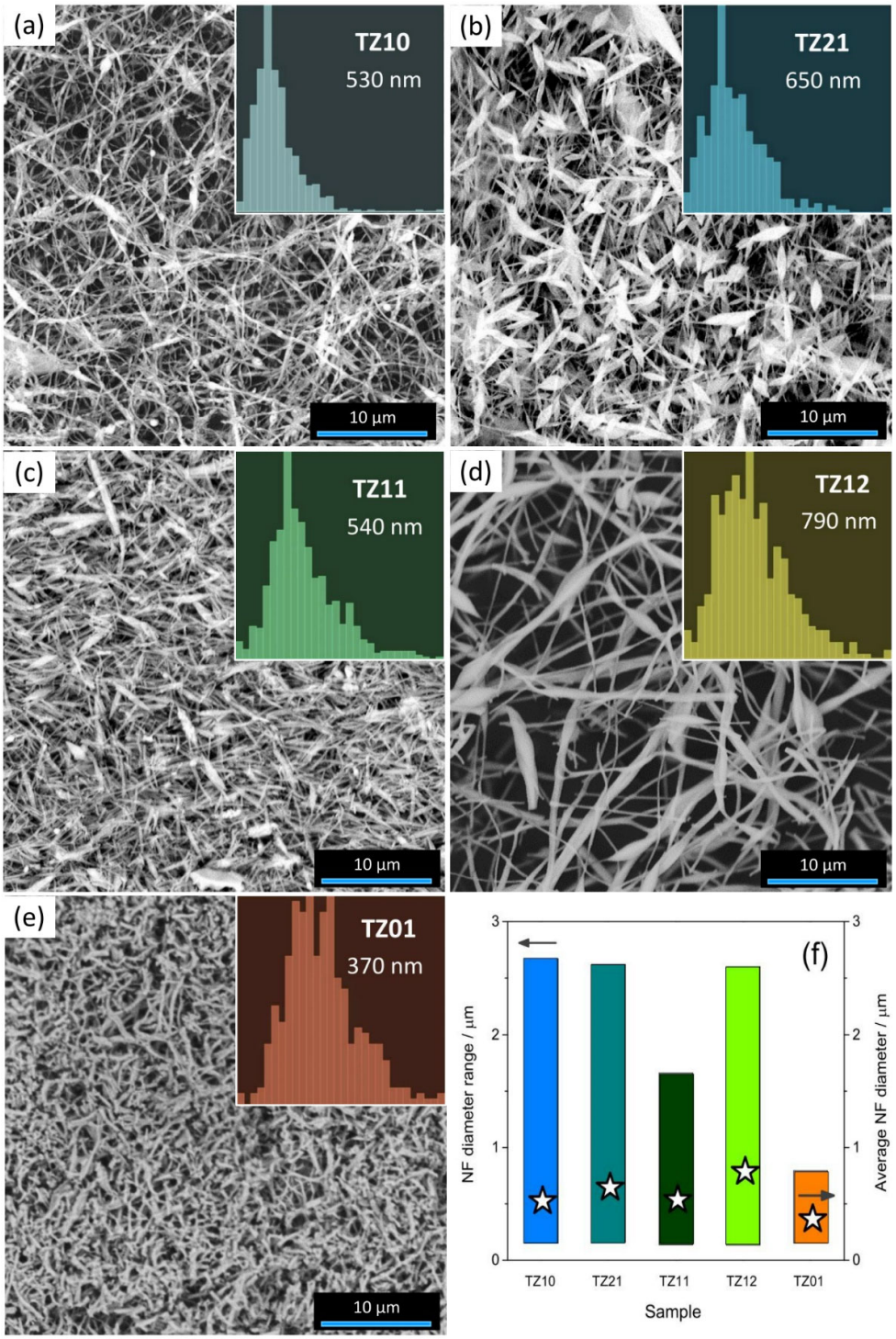

Figure 1. Results of the SEM analysis. (**a**–**e**) SEM micrograph of photocatalysts (**a**) TZ10, (**b**) TZ21, (**c**) TZ11, (**d**) TZ12, and (**e**) TZ01 (insets: NF diameter distributions); (**f**) range and average value of the NF diameter.

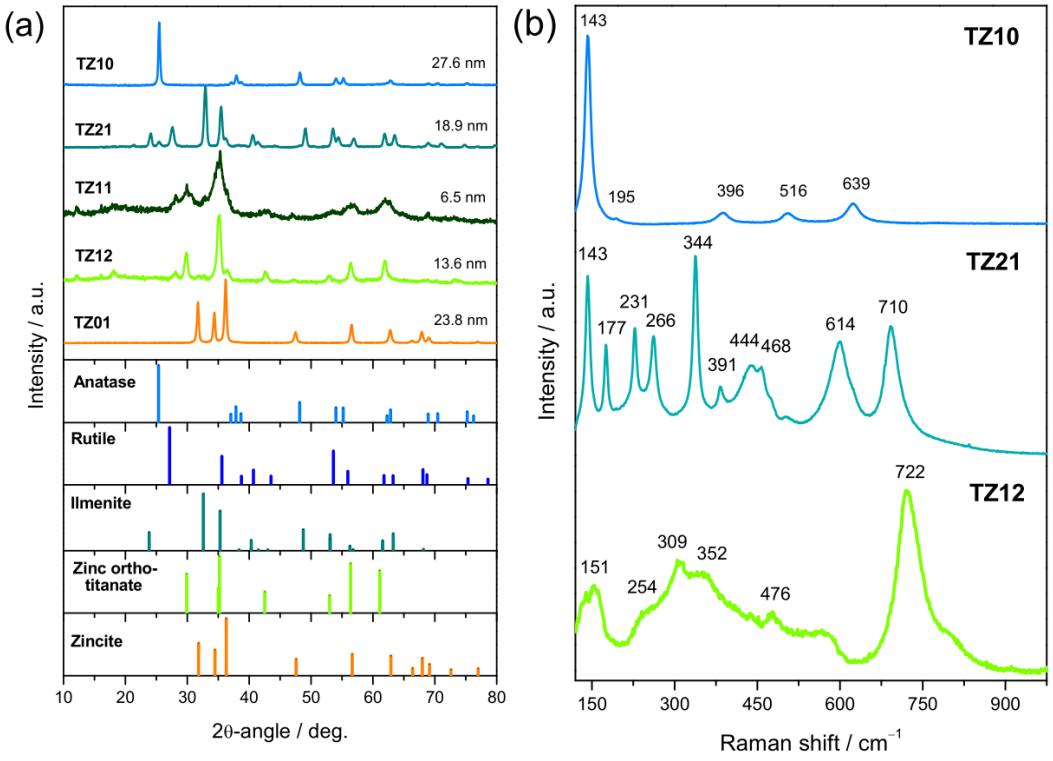

Figure 2. Results of (**a**) XRPD and (**b**) MRS analyses.

The spatial homogeneity of the samples and their crystallinity degree were evaluated by MRS (Figures 2b and S3). The comparison among the spectra recorded at different random positions in each sample (Figure S3) reveals the lack of appreciable shifts in the positions and relative intensities of the peaks. This finding indicates that the produced photocatalysts are featured by high spatial uniformity. Figure 2b displays their averaged micro-Raman spectra. In agreement with the indications emerging from the XRPD analysis, the lowest crystallinity degree pertains to sample TZ11, whose spectra exhibit no evident Raman peak and an intense photoluminescence (PL) background (Figure S3c). In accordance with previous studies [21,46], an intense PL background, originating from point defects and non-stoichiometry, is present also in the spectrum of sample TZ01 (not shown here), where the E_2(high) and E_2(low) modes, arising from the motion of the O atoms and the vibrations of Zn sub-lattice in the hexagonal ZnO structure (space group $P6_3mc$), are detected at 441 and 584 cm^{-1}, respectively [52]. In the spectrum of sample TZ10, the Raman active modes of tetragonal anatase (space group $I4_1/amd$) are detected at 143 cm^{-1} (E_g), 195 cm^{-1} (E_g), 396 cm^{-1} (B_{1g}), 517 cm^{-1} (A_{1g}-B_{1g}), and 639 cm^{-1} (E_g) [53,54]. The spectrum of sample TZ21 exhibits ten peaks at 143, 177, 231, 266, 344, 391, 444, 468, 614, and 710 cm^{-1}. They arise from the $E_g(1)$, $A_g(1)$, $E_g(2)$, $A_g(2)$, $A_g(3)$, $E_g(3)$, $E_g(4)$, $A_g(4)$, $E_g(5)$, and $A_g(5)$ symmetrical phonon modes of $ZnTiO_3$ (space group R3 No. 148) [55]. The downshift of the higher frequency modes hints at the occurrence of tensile strain within the NFs. Five peaks originating from the $F_{2g}(1)$, E_g, $F_{2g}(2)$, $F_{2g}(3)$, and A_{1g} phonon modes of the inverse spinel Zn_2TiO_4 (space group O_h^7-Fd3m) are detected in the spectrum of sample TZ12, at 254, 309, 352, 476, and 722 cm^{-1}, respectively [49,55]. Besides, the detection of a peak ascribable to the A_{1g} mode of titania with r-TiO_2 structure at 151 cm^{-1} [49] confirms the formation of a secondary phase in this sample.

3.3. Effect of the Variation of the Ti:Zn Molar Ratio in the Precursor Solution on the Photocatalytic Activity of the Resulting Electrospun Oxide NFs

The photocatalytic activity of the set of samples produced from precursor solutions with different Ti:Zn molar ratios toward the degradation of MB was evaluated at RT. This was accomplished by dispersing the as-calcined oxide NFs (0.33 mg mL^{-1}) in an aqueous MB solution with an initial concentration of 15 μM and measuring the absorbance after exposure to 350 nm (3.54 eV) UV radiation for given time intervals. Figure S4 displays the spectrum of the as-prepared aqueous MB solution. Two absorption bands, peculiar to MB [56], are observed at 291 and 664 nm, with two weaker characteristic contributions at 247 and 617 nm. The most intense absorption band arises from n-π* vibronic transitions, while π–π* transitions are responsible for the detection of the band at 291 nm [56]. With increasing irradiation time, the intensity of absorption bands progressively weakens, indicating that the cationic dye gradually degrades. Figure 3a–e displays the time evolution of the strongest MB absorption band, as measured in the presence of the investigated photocatalysts. As usual [21,28], the ratio between absorbance at an irradiation time t (A_t) and initial absorbance (A_0), both measured at 664 nm wavelength, was utilized to estimate the percentage of dye degradation as $D = 100 \cdot (1 - A_t/A_0)$. The obtained results are shown in Figure 3f and compared with the literature ones in Table S1.

Many groups have reported that photocatalysts based on Ti- and Zn-oxides exhibit better performance with respect to both TiO_2 and ZnO [26,28,30]. Contrary to expectations, all the Ti/Zn-oxide NFs (samples TZ21, TZ11, and TZ12) under evaluation exhibit lower activity compared to the TiO_2 and ZnO NFs (samples TZ10 and TZ01, respectively). At any time, the lowest degradation rate pertains to sample TZ11. After 2 h, only 12% MB has degraded, whereas photocatalysts prepared via hydrothermal method from $ZnCl_2$ and $TiCl_4$ in a 1:1 molar ratio exhibit better performance [30]. Samples TZ12 and TZ21 exhibit activities towards the dye solution discoloration similar to each other. Their degradation rates are 41 and 42% after 2 h, respectively. After 3 h, D rises up to 56 and 59% (for TZ21 and TZ12, respectively), reaching values falling in the range of those obtained, in the same time, with a greatly higher concentration (10 mg mL^{-1}) of electrospun Ti-Zn complex oxide NFs produced from different precursors (see entry 4 in Table S1) [27].

As known [47], the photocatalytic performance strongly depends on the specific surface area: as a general trend, the larger the specific surface area, the greater the number of available sites for the adsorption of the dye molecules and, hence, the higher the catalytic activity. Chemical etching with a strong base is a strategy commonly adopted to increase the surface area of nanomaterials [45,47]. For this purpose, after calcination, a portion of sample TZ21 was treated with a NaOH solution, as described in Section 2.2.

The treatment did not alter either the morphology (Figure S5) or the crystalline phase of the oxide (Figure S6). It resulted in NF thinning (the center of the NF diameter distribution moved from 650 to 550 nm), average crystallite size increase (from 19 to 27 nm) due to the selective removal of defective surface oxide regions and Na-incorporation, as suggested by the downshift of the strongest diffraction peaks (inset of Figure S6) and confirmed by the results of the elemental mapping via SEM/EDX (Figure S5). Although the treatment with NaOH produces a notable increase in the surface area [47], the activity of the chemically etched photocatalyst (coded as TZ21NaOH) improves only to a limited extent with respect to that of the un-etched one (Figure S7). After 2 h, 51% (against 42%) MB has degraded. This finding indicates that specific surface area is not the factor mostly limiting the photocatalytic activity of the sample towards the dye degradation.

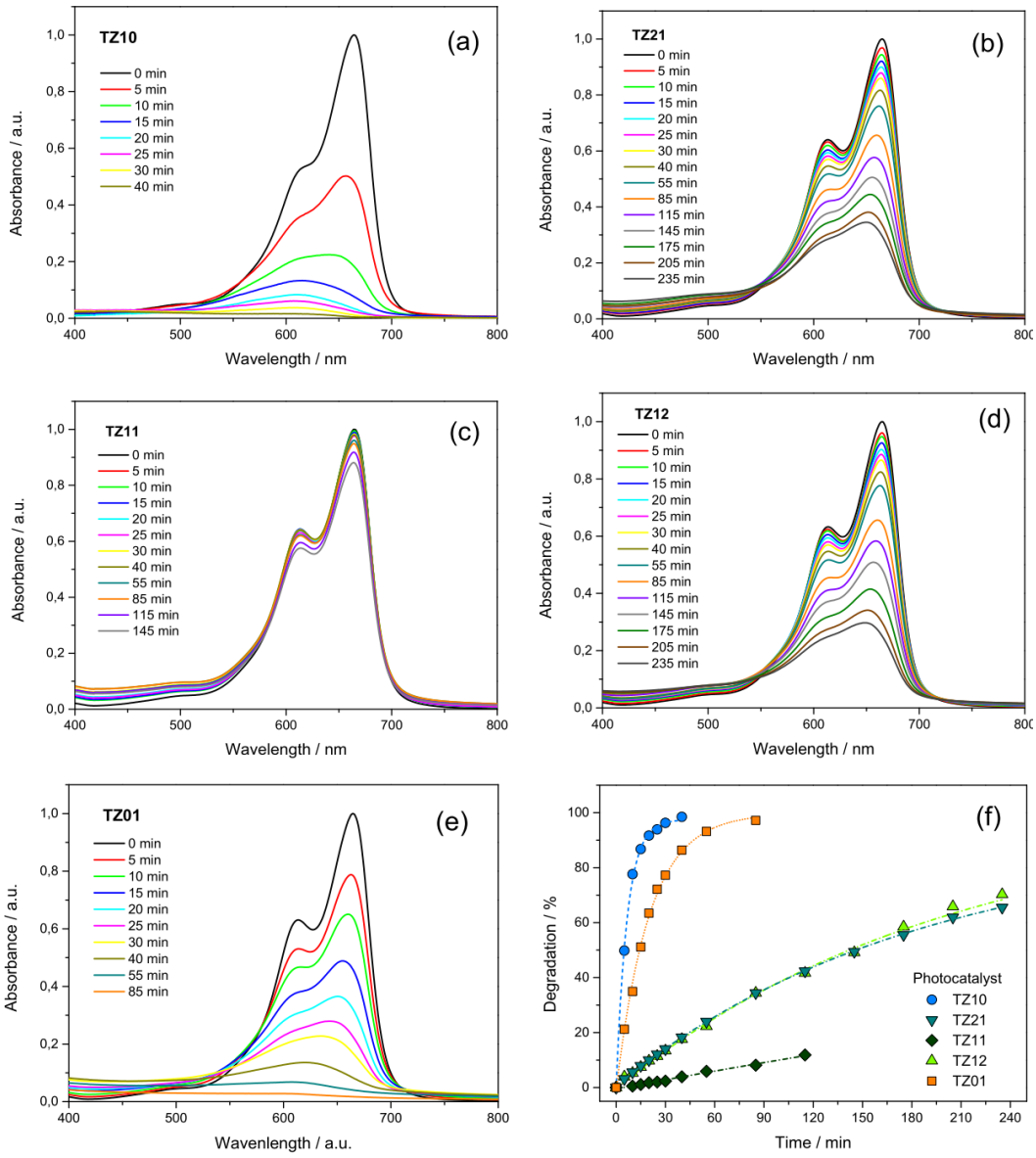

Figure 3. Effect of the variation of the Ti:Zn molar ratio in the precursor solution on the photocatalytic performance of the resulting oxide NFs. (**a**–**e**) Time–evolution of the absorbance spectra of an aqueous MB solution with initial concentration of 15 μM and catalyst load of 0.33 mg mL^{-1}, under exposure to 350 nm UV radiation; the shown spectra refer to photocatalysts (**a**) TZ10, (**b**) TZ21, (**c**) TZ11, (**d**) TZ12, and (**e**) TZ01. (**f**) Corresponding degradation rates as a function of time.

ZnO–TiO_2 nanocomposites, prepared by hydrothermal [29,30] or solvothermal method [57], have been reported to catalyze the MB degradation process under irradiation with VIS light, showing high reaction rate constants (3.00–6.52 × 10^{-1} min^{-1}, under irradiation with 862 W cm^{-2} sunlight) [29] and better performance with respect to both ZnO and TiO_2 alone (compare entries 12–16 in Table S1) [30,57]. Hence, the photocatalytic activity of the present Ti/Zn-oxide NFs toward the degradation of MB was evaluated under exposure to 550 nm (2.25 eV) VIS light. Figure S8 shows the results obtained by dispersing 0.33 mg mL^{-1} TZ12 and TZ21NaOH in an aqueous MB solution with a 15 μM initial concentration. Sample TZ12 is practically photocatalytically inactive. The activity of sample TZ12 is very low: after 2 h, *D* is <9%. This suggests that VIS light does not have sufficient energy to activate the catalyst by generating the electron–hole pairs necessary for the redox reactions with the species adsorbed on its surface [32–34].

At underexposure with higher energy radiation (3.54 against 2.25 eV), the activity of the present electrospun NFs toward the degradation of MB improves in the order TZ11 < TZ12 ≅ TZ21 < TZ01 < TZ10 (Figure 3f). In particular, sample TZ10 (*a*-TiO_2) fully discolors the MB solution in only 40 min (D = 99%). In the same time interval, 86% MB has degraded by the use of sample TZ01 (ZnO). On the contrary, when samples TZ21 ($ZnTiO_3$), TZ12 (chiefly Zn_2TiO_4), and TZ11 (highly disordered Zn_2TiO_4) are utilized as catalysts, after 40 min, most of the dye (81.7, 82.4 and 96.1%, respectively) is still present in the solution. The better performance of both the binary oxide NFs is in line with the reports by Kim et al. [27] on Ti/Zn oxide NFs prepared via ES by using different precursors. The trend observed in terms of photocatalytic activity improvement well correlates with the energy gap of the samples, which increases in the order TiO_2 (3.20 and 3.00 eV for anatase and rutile phase, respectively [28,58]) < ZnO (3.37 eV [59]) < $ZnTiO_3$ (3.67 eV [48]) < Zn_2TiO_4 (4.01eV [60]). The smaller the gap, the more active the catalyst.

The formation of high-gap ternary oxides ($ZnTiO_3$ and Zn_2TiO_4) is favored by the thermal treatment at 600°C, a temperature that allows removing the organic constituents from the precursors NFs and crystallizing the oxide nanocrystals. Indeed, $Zn_2Ti_3O_8$ and Zn_2TiO_4 NRs have been obtained, upon calcination at high temperature, from ZnO NRs decorated with TiO_2 NPs prepared by hydrothermal method. Their formation has been attributed to the different diffusion rates of Ti^{4+} and Zn^{2+} ions [50].

Besides, the crystallinity degree of the sample also matters. Mekasuwandumrong et al. [61] have shown that the photocatalytic activity of ZnO nanoparticles synthesized via flame-spray pyrolysis improves with the crystalline quality of the oxide, as assessed via the XRPD analysis. The larger the average crystallite size, the higher the activity in the degradation of MB [61]. In the present case, based on the d_C values inferred from the XRPD analysis (Figure 2a), the crystalline quality of the oxides improves in the order TZ11 < TZ12 < TZ21 < TZ01 < TZ10, i.e., consistently with the improvement order of the activity of the oxide NFs (TZ11 < TZ12 ≅ TZ21 < TZ01 < TZ10).

In the following, attention is focused on *a*-TiO_2 and ZnO NFs that outperform not only the Ti/Zn-oxide NFs, as above discussed, but also most state-of-art anatase and zinc oxide photocatalysts. This important feature is detailed in the next Section.

3.4. Effect of the Photocatalyst Load

Determining the optimum photocatalyst concentration is of crucial importance since it allows scaling up the process, with relevant impact on the economic aspects of the whole discoloration process. Accordingly, we have investigated the effect of the photocatalyst load (0.10, 0.33, 0.66 or 1.00 mg mL^{-1}) on the dye degradation efficiency. Proper amounts of *a*-TiO_2 or ZnO NFs were dispersed in the MB solution and activity was evaluated at RT under UV irradiation. Figure 4a–c displays the absorbance spectra recorded at different time intervals in the presence of 0.10, 0.66 and 1.00 mg mL^{-1} *a*-TiO_2 NFs (photocatalyst TZ10); the corresponding time–evolution of the degradation rates is shown in Figure 4d and a larger time interval is displayed in Figure S9. Sample TZ10 exhibits outstanding degradation performance, compared with both electrospun titania NFs and TiO_2 photocatalysts prepared by different techniques (compare entries 17–20 with 1, 3, 6, 16 and 32–35 in Table S1). Just to cite some D values, at the lowest concentration (0.1 mg mL^{-1}), the percentage of dye degraded after 4 h (94%) exceeds by a factor greater than 4.5 that reported by Lee et al. [26] for a higher load of electrospun titania NFs in the same time interval (see entry 1 in Table S1). At 0.66 and 1.00 mg mL^{-1} loads, respectively 97% and 99% MB decomposes in less than 2 h, while, according to reports by Kim et al. [27], 93% dye removal from a solution with the same initial concentration is achieved in a longer time by the use of a largely higher concentration of electrospun titania NFs (see entry 3 in Table S1).

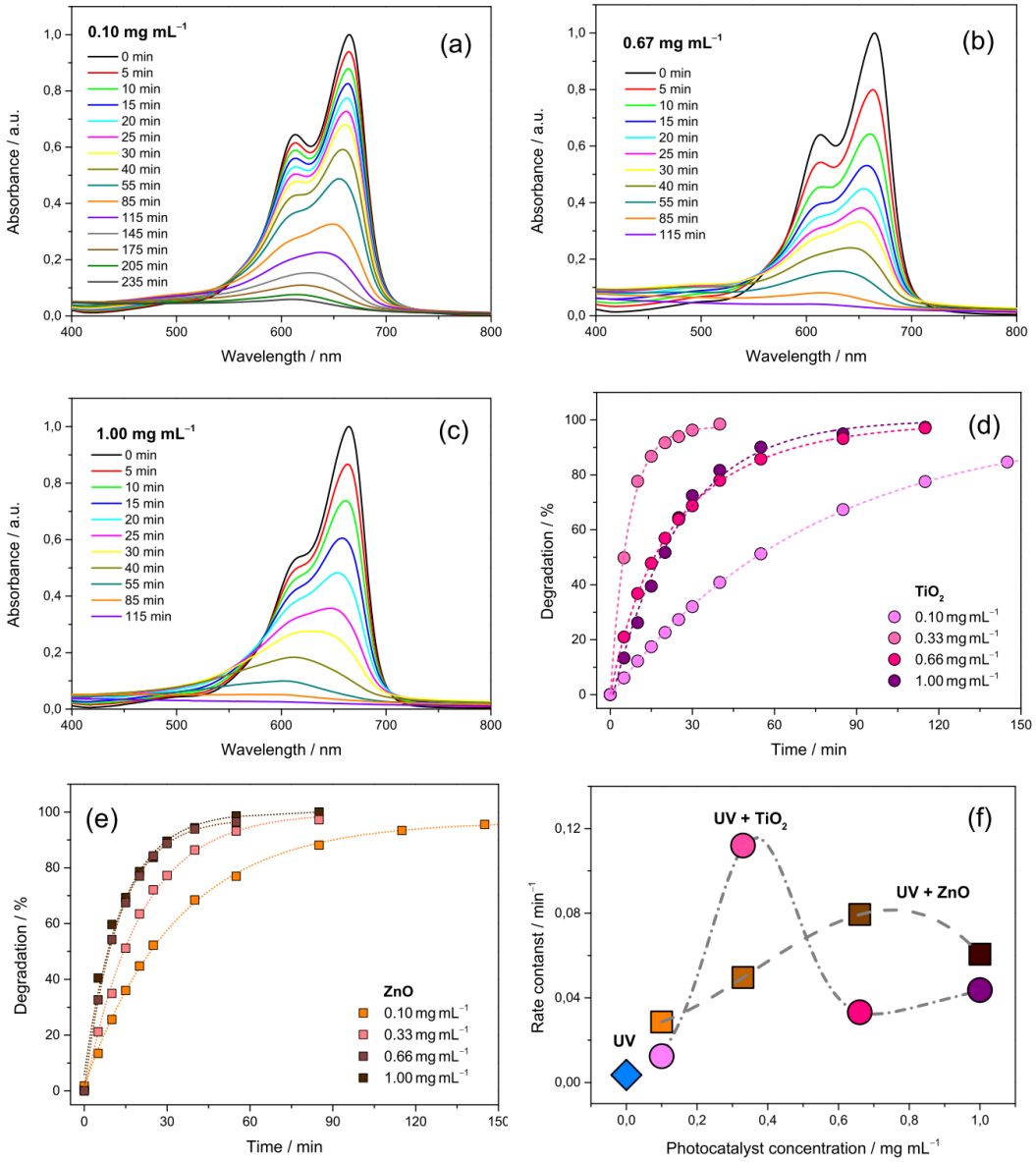

Figure 4. Effect of the load of the electrospun NFs on the photocatalytic performance of *a*-TiO_2 NFs and ZnO NFs. (**a–c**) Time–evolution of the absorbance spectra of an aqueous MB solution with initial 15 μM concentration and different concentrations of *a*-TiO_2 NFs, under exposure to 350 nm UV radiation. (**d**,**e**) Degradation rates of photocatalysts (**d**) TZ10 and (**e**) TZ01 as a function of time. (**f**) Concentration-dependence of the corresponding rate constants.

The time–evolution of the degradation rates for ZnO NFs (photocatalyst TZ01) is shown in Figure 4e. The absorbance spectra recorded in the presence of 0.66 mg mL^{-1} are displayed in Figure S10. Those relative to 0.1 and 1.0 mg mL^{-1} loads were reported in previous work [21]. At the lower concentrations (0.10 and 0.33 mg mL^{-1}), 89% and 97% MB degrades in less than 1.5 h, while in the same interval lower *D* values are reported by other authors (see entry 7 in Table S1). By using higher loads of ZnO NFs (0.66 mg mL^{-1}), the MB solution fully discolors in less 1 h.

In order to calculate the reaction rate constants, the A_t/A_0 ratios between absorbance measured at 664 nm, at equilibrium, at times *t* and 0, were plotted in a semi-logarithmic scale as a function of the irradiation time, as shown in Figure S11 for *a*-TiO_2 NFs at different loads. Regardless of the photocatalyst concentration, linear trends were found, as in the case

of UV radiation alone. This finding indicates that the kinetics of the process can be modeled via a pseudo first-order law [5,21]. The values of the rate constants (k), obtained as the slope of the curves $\ln(A_t/A_0) = -k\,t$ via a best-fit procedure to the data, are reported in Table S1 (entries 17–20 and 27–30). The k-values for a-TiO_2 (1.24×10^{-2}–1.12×10^{-1} min^{-1}) and ZnO NFs (2.86×10^{-2}–7.94×10^{-2} min^{-1}) well compare with those available in the literature for titania and zincite photocatalysts (see entries 12, 16 and 32–35 in Table S1).

Figure 4f displays the load dependence of the reaction rate constants for photocatalysts TZ10 and TZ01. Although the details are different, in both cases, k varies non-monotonically with the catalysts concentration, in line with reports by other authors [62,63]. The curve relative to a-TiO_2 NFs exhibits a sharp maximum at 0.33 mg mL^{-1}; in the case of the ZnO NFs, the variation of k with the photocatalyst load is smoother and the optimal load value is higher (0.66 mg mL^{-1}). However, in both cases, very small relative amounts of the photocatalyst, compared to those frequently utilized [26,27,57], allow the dye to be effectively degraded. The initial improvement in the discoloration efficiency reflects the increase in the number of the photocatalyst active sites and the consequent enhancement in the formation of the hydroxyl ($OH^{\bullet}$) and superoxide ($O_2^{\bullet}$) radicals, responsible for the dye degradation [62,63]. The worsening at higher loads may be due to two cooperative mechanisms [62,63]. On one hand, a higher concentration of the active material favors the agglomeration of the catalyst NPs/NFs, which reduces the active surface area. On the other hand, it reflects on greater turbidity of the catalyst suspension, which increasingly hampers the light penetration.

It is worth noticing that, after load optimization, for ZnO NFs, a significant improvement with respect to the previously reported results [21] is obtained (namely, a rate constant of 7.94×10^{-2} min^{-1} for 0.66 mg mL^{-1} load against 6.06 min^{-1} for 1.00 mg mL^{-1}). This finding (i.e., higher activity with lower load) may be useful to scale up the process on an industrial scale. Outstandingly, a-TiO_2 NFs exhibit even higher activity toward the MB degradation ($k = 1.12 \times 10^{-1}$ min^{-1}) at a smaller load (0.33 mg mL^{-1}) compared to ZnO NFs.

3.5. On the Best Performing Oxide NFs

The outstanding photocatalytic behavior of sample TZ01 has been previously discussed [21]. It is due to the architecture of the NFs, consisting of interconnected polycrystalline nanoplatelets, with defects (located at the grain boundaries) that, acting as traps for the photogenerated e^--h^+ pairs, reduce the rate for their recombination and make them available for the reduction and oxidation reactions.

In this work, we focused on a-TiO_2 NFs, which at the optimal load (0.33 mg mL^{-1}) exhibit higher activity toward the MB degradation ($k = 1.12 \times 10^{-1}$ min^{-1}, i.e., 6.72 h^{-1}) compared to P25-TiO_2, a mixture of anatase and more active rutile, commonly regarded as the photocatalysis benchmark (e.g., $k = 1.46$ h^{-1} for P25 NPs [64] and $k = 5.02 \times 10^{-2}$ min^{-1} for P25 NPs immobilized into a thin electrospun polymer mat [65]). A deeper insight into its morphology was achieved by carrying out an AFM analysis. Figures 5a and S12a show representative topographic images of the NPs composing the NFs, as obtained after the dissolution of the NFs in acetone. The distributions of the diameters and heights of the NPs, as resulting from the statistical analysis of the topographic images, are shown in Figure 5b,c, respectively. These results validate those previously obtained on the ZnO NFs [21]. As designed, the architecture of a-TiO_2 NFs consists of interconnected oxide NPs (compare Figure S12c,d,g with Figure S12e,f,h, respectively). Anatase NPs are polycrystalline in nature (the average NP size exceeds the average crystallite size) and larger in diameter with respect to the ZnO ones (69 ± 13 nm against 47 ± 6 nm). The bi-modal distribution of the NP heights indicates that the a-TiO_2 NFs NF is constituted by both thinner and thicker NPs (mainly 8.0 ± 0.5 nm and 13.1 ± 1.3 nm in height) compared to ZnO platelets (9.3 ± 1.3 nm in height) [21].

Additional information about photocatalyst TZ10 is inferred from the high magnification SEM/EDX analysis (Figure S13). The analysis reveals the successful achievement of sub-stoichiometric titania oxide ($TiO_{1.9}$). The oxygen-deficiency of the

oxide (5%), which is beneficial for the photocatalytic activity [20,21,66], is further confirmed by the results of the quantitative analysis of the micro-Raman spectra of the sample (Figure S14 and Table S2). As known [67–69], the lowest frequency E_g peak of anatase may blue-shift and broaden (with respect to bulk) owing to phonon confinement effects arising from finite size of the oxide grains (<10 nm) or shortening of the correlation length due to the presence of defects and non-stoichiometry. Since the crystallite size resulting from XRPD data (27.6 nm) rules out the occurrence of finite-size effects, the presence of localized defects, i.e., oxygen vacancies and interstitials mainly located at the grain boundaries [20,21], is responsible for the broadening of the peak (13.7 against 7.6 cm^{-1}) with respect to oxide nanocrystals having similar size [67].

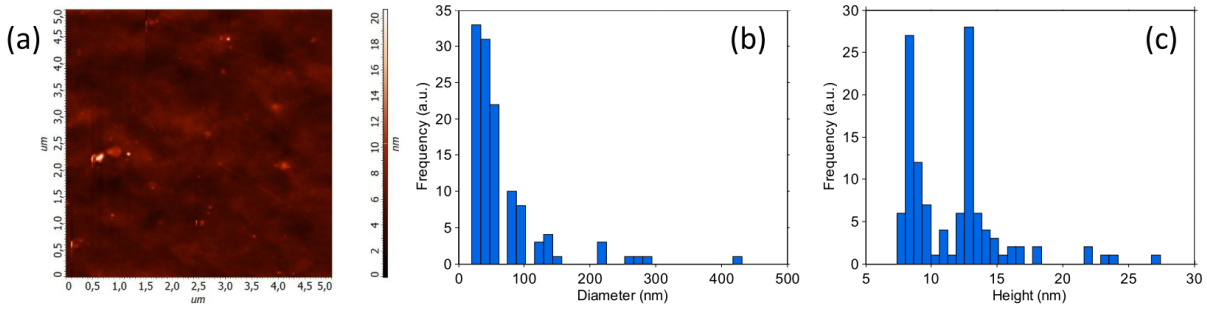

Figure 5. (**a**) Representative AFM image of NF-composing nanoparticles in sample TZ10. (**b**) Diameter and (**c**) height distributions.

Last, but not least, we have assessed the stability and reusability of the best performing photocatalyst (TZ10) under optimal conditions (0.33 mg mL^{-1} load). Reusability of the catalyst is an important aspect of the heterogeneous catalysis process to which industries are particularly interested. The reuse generally involves filtration and/or centrifugation to separate it from the reaction medium and regeneration via washing with proper liquids or heat treatment to remove from its surface intermediates, often responsible for its deactivation/poisoning [70,71]. These complex and time-consuming procedures impact the costs of the process [70]. In this work, we demonstrate that the catalyst can be reused *without* separating it from the reaction medium or washing it with water or other liquids. The initial concentration of the dye (15 μM) was restored by adding the proper amount of MB to the discolored solution. Cycling tests were done by monitoring the decrease in MB concentration under the same reaction conditions as during the first use. The results (Figure S15) indicate that, under the above-described conditions, the activity of oxygen-deficient *a*-TiO_2 NFs decreases moderately (after 40 min, *D* reduces from 98.5% in the first cycle to 93.4% and 75.9% in the second and third ones, respectively).

4. Conclusions

Binary (anatase TiO_2 and wurtzite ZnO) and ternary ($ZnTiO_3$ and Zn_2TiO_4) oxide NFs with engineered architecture and surface were prepared via electrospinning and subsequent calcination from precursor solutions with different Ti:Zn molar ratios. The comparative evaluation of the as-calcined NFs as photocatalysts for the removal of MB from an aqueous solution with a dye concentration of 15 μM under UV irradiation indicates that the higher band gap and lower crystallinity of the ternary oxides reflect in a lower photocatalytic activity towards the dye degradation. Capture centers generated by properly tuning the preparation conditions were responsible for the very high activity of the binary oxide nanofibers. Their optimal loads were determined to maximize the efficiency of the photocatalytic process, which is a fundamental recipe for its industrial use.

By optimizing the load of wurtzite ZnO NFs (0.66 mg mL^{-1}), a higher rate constant (7.94×10^{-2} min^{-1}) than previously reported was achieved. More importantly, when anatase TiO_2 NFs are used, optimizing the efficiency of the photodegradation process

requires a lower catalyst load (0.33 mg mL^{-1}) and, besides, the reaction rate constant (1.12 × 10^{-1} min^{-1}) exceeds most of the values reported for state-of-art electrospun photocatalysts and for the commonly used P25-TiO_2 benchmark, as well. This behavior is due to the NF architecture and the presence of oxygen vacancies acting as capture-centers to reduce the recombination rate of the photogenerated e^--h^+ pairs. This finding proves the wider validity of the conclusions previously drawn on the key role of defects in the design of ZnO photocatalyst.

By using only 0.33 mg mL^{-1} oxygen-deficient *a*-TiO_2 NFs, the solution fully discolors after 40 min. Remarkably, after reuse without any regeneration procedure, their activity in the second cycle decreases only by 5.2%. In the third one, it further undergoes a diminishing of 18.7%. This result opens the path for industries to lower their operational cost of the large-scale process cleaning waters from MB dye.

This laboratory-scale study highlights the crucial importance of determining the optimal concentration of the photocatalyst, proving that very small relative amounts of it allow the dye to be effectively degraded. Furthermore, thanks to the scalability of the electrospinning technique, it provides a new perspective towards the sustainable large-scale manufacture of photocatalysts for the treatment of industry effluents.

Supplementary Materials: The following are available online at www.mdpi.com/article/10.3390/app11209720/s1, Figure S1: Sketch of the activation of the catalyst; Figure S2: Results of the SEM/EDX analysis; Figure S3: Micro-Raman spectra; Figure S4: Absorbance spectrum of aqueous MB solution; Figure S5: Results of the SEM/EDX analysis on sample TZ21NaOH; Figure S6: Results of XRPD analysis on sample TZ21 before and after chemical etching by NaOH; Figure S7: Absorbance spectra recorded at different time intervals under UV radiation with photocatalyst TZ21NaOH and time–evolution of the corresponding degradation rate; Figure S8: Absorbance spectra recorded at different time intervals under VIS radiation with photocatalysts TZ12 and TZ21NaOH; Figure S9: Time–evolution of the degradation rates under UV radiation for different loads of photocatalyst TZ10; Figure S10: Absorbance spectra recorded at different time intervals under UV radiation with photocatalyst TZ01; Figure S11: Semi-logarithmic plot of A_t/A_0 ratio as a function of irradiation time for photocatalyst TZ10; Figure S12: AFM images of NF-composing nanoparticles in samples TZ10 and diameter and height distributions of the NF-composing NPs for samples TZ10 and TZ01; Figure S13: High magnification SEM image and SEM/EDX spectrum of sample TZ10; Figure S14: Anatase structure fit to the micro Raman spectrum of sample TZ10; Figure S15: Reusability test for photocatalyst TZ10; Table S1: MB degradation performance of TiO_2/ZnO-based photocalysts; Table S2: Results of the fitting procedure for the micro-Raman spectrum of sample TZ10.

Author Contributions: Conceptualization, S.P. and S.S.; methodology, B.P., Z.D., C.T., F.P. and A.M.; validation and formal analysis, Z.D., C.T. and F.P.; data curation C.T. and S.S.; writing—original draft preparation C.T. and S.S.; writing—review and editing, S.P., M.A. and S.S. All authors have read and agreed to the published version of the manuscript.

Funding: This research received no external funding.

Institutional Review Board Statement: Not applicable.

Informed Consent Statement: Not applicable.

Data Availability Statement: The raw data and processing aids, required to reproduce the findings of this work, cannot be shared at this time as they form the basis for an ongoing study.

Conflicts of Interest: The authors declare no conflict of interest.

References

1. UN. Historic New Sustainable Development Agenda Unanimously Adopted by 193 UN Members. 2015. Available online: https://www.un.org/sustainabledevelopment/blog/2015/09/historic-new-sustainable-development-agenda-unanimously-adopted-by-193-un-members (accessed on 1 September 2021).
2. Fito, J.; Abrham, S.; Angassa, K. Adsorption of methylene blue from textile industrial wastewater onto activated carbon of Parthenium hysterophorus. *Int. J. Environ. Res.* **2020**, *14*, 501–511. https://doi.org/10.1007/s41742-020-00273-2.

3. Mahvi, A.H.; Ghanbarian, M.; Nasseri, S.; Khairi, A. Mineralization and discoloration of textile wastewater by TiO_2 nanoparticles. *Desalination* **2009**, *239*, 309–316. https://doi.org/10.1016/j.desal.2008.04.002.
4. Lellis, B.; Fávaro-Polonio, C.Z.; Pamphile, J.A.; Polonio, J.C. Effects of textile dyes on health and the environment and bioremediation potential of living organisms. *Biotechnol. Res. Innov.* **2019**, *3*, 275–290. https://doi.org/10.1016/j.biori.2019.09.001.
5. Balcha, A.; Yadav, O.P.; Dey, T. Photocatalytic degradation of methylene blue dye by zinc oxide nanoparticles obtained from precipitation and sol-gel methods. *Environ. Sci. Pollut. Res.* **2016**, *23*, 25485–25493. https://doi.org/10.1007/s11356-016-7750-6.
6. Zamel, D.; Khan, A.U. Bacterial immobilization on cellulose acetate based nanofibers for methylene blue removal from wastewater: Mini-review. *Inorg. Chem. Commun.* **2021**, *131*, 108766. https://doi.org/10.1016/j.inoche.2021.108766.
7. Methylene Blue Market Size, Industry Analysis Report, Regional Outlook, Application Development Potential, Price Trends, Competitive Market Share & Forecast, 2021–2027. Available online: https://www.gminsights.com/industry-analysis/methylene-blue-market (accessed on 30 July 2021).
8. Singh, J.; Chang, Y.Y.; Koduru, J.R.; Yang, J.K. Potential degradation of methylene blue (MB) by nano-metallic particles: A kinetic study and possible mechanism of MB degradation. *Environ. Eng. Res.* **2018**, *23*, 1–9. https://doi.org/10.4491/EER.2016.158.
9. Vaiano, V.; Iervolino, G.; Rizzo, L.; Sannino, D. Advanced oxidation processes for the removal of food dyes in wastewater. *Curr. Org. Chem.* **2017**, *21*, 1068–1073. https://doi.org/10.2174/1385272821666170102163307.
10. Sharma, V.K.; Feng, M. Water depollution using metal-organic frameworks-catalyzed advanced oxidation processes: A review. *J. Hazard. Mater.* **2019**, *372*, 3–16. https://doi.org/10.1016/j.jhazmat.2017.09.043.
11. Sales, H.B.; Menezes, R.R.; Neves, G.A.; de Souza, J.J.; Ferreira, J.M.; Chantelle, L.; Lira, H.D.L. Development of sustainable heterogeneous catalysts for the photocatalytic treatment of effluents. *Sustainability* **2020**, *12*, 7393. https://doi.org/10.3390/su12187393.
12. Zheng, F.; Zhu, Z. Flexible, freestanding, and functional SiO2 nanofibrous mat for dye-sensitized solar cell and photocatalytic dye degradation. *ACS Appl. Nano Mater.* **2018**, *1*, 1141–1149. https://doi.org/10.1021/acsanm.7b00316.
13. Ali, G.; Jazib Abbas Zaidi, S.; Abdul Basit, M.; Joo Park, T. Synergetic Performance of Systematically Designed g-C_3N_4/rGO/SnO_2 Nanocomposite for Photodegradation of Rhodamine-B Dye. *Appl. Surf. Sci.* **2021**, *570*, 151140. https://doi.org/10.1016/j.apsusc.2021.151140.
14. Zhao, Q.; Wang, K.; Wang, J.; Guo, Y.; Yoshida, A.; Abudula, A.; Guan, G. Cu_2O Nanoparticle Hyper-Cross-Linked Polymer Composites for the Visible-Light Photocatalytic Degradation of Methyl Orange. *ACS Appl. Nano Mater.* **2019**, *2*, 2706–2712. https://doi.org/10.1021/acsanm.9b00210.
15. Gnanasekaran, L.; Hemamalini, R.; Saravanan, R.; Ravichandran, K.; Gracia, F.; Agarwal, S.; Gupta, V.K. Synthesis and characterization of metal oxides (CeO_2, CuO, NiO, Mn_3O_4, SnO_2 and ZnO) nanoparticles as photo catalysts for degradation of textile dyes. *J. Photochem. Photobiol. B* **2017**, *173*, 43–49. https://doi.org/10.1016/j.jphotobiol.2017.05.027.
16. Wang, X.T.; Li, Y.; Zhang, X.Q.; Li, J.F.; Li, X.; Wang, C.W. Design and fabrication of NiS/LaFeO3 heterostructures for high efficient photodegradation of organic dyes. *Appl. Surf. Sci.* **2020**, *504*, 144363. https://doi.org/10.1016/j.apsusc.2019.144363.
17. Chen, H.; Motuzas, J.; Martens, W.; da Costa, J.C.D. Degradation of orange II dye under dark ambient conditions by MeSrCuO (Me= Mg and Ce) metal oxides. *Sep. Purif. Technol.* **2018**, *205*, 293–301. https://doi.org/10.1016/j.seppur.2018.05.029.
18. Mageshwari, K.; Sathyamoorthy, R.; Lee, J.Y.; Park, J. Novel $CuCr_2O_4$ embedded CuO nanocomposites for efficient photodegradation of organic dyes. *Appl. Surf. Sci.* **2015**, *353*, 95–102. https://doi.org/10.1016/j.apsusc.2015.06.027.
19. Ramar, V.; Balasubramanian, K. Reduced Graphene Oxide/WO_3 Nanorod Composites for Photocatalytic Degradation of Methylene Blue under Sunlight Irradiation. *ACS Appl. Nano Mater.* **2021**. https://doi.org/10.1021/acsanm.1c00863.
20. Senthamizhan, A.; Balusamy, B.; Aytac, Z.; Uyar, T. Grain boundary engineering in electrospun ZnO nanostructures as promising photocatalysts. *CrystEngComm* **2016**, *18*, 6341–6351. https://doi.org/10.1039/c6ce00693k.
21. Pantò, F.; Dahrouch, Z.; Saha, A.; Patanè, S.; Santangelo, S.; Triolo, C. Photocatalytic degradation of methylene blue dye by porous zinc oxide nanofibers prepared via electrospinning: When defects become merits. *Appl. Surf. Sci.* **2021**, *557*, 149830. https://doi.org/10.1016/j.apsusc.2021.149830.
22. Phuruangrat, A.; Kuntalue, B.; Thongtem, S.; Thongtem, T. Hydrothermal synthesis of hexagonal ZnO nanoplates used for photodegradation of methylene blue. *Optik* **2021**, *226*, 165949. https://doi.org/10.1016/j.ijleo.2020.165949.
23. Reza, K.M.; Kurny, A.S.W.; Gulshan, F. Parameters affecting the photocatalytic degradation of dyes using TiO_2: A review. *Appl. Water Sci.* **2017**, *7*, 1569–1578. https://doi.org/10.1007/s13201-015-0367-y.
24. Ishchenko, O.M.; Lamblin, G.; Guillot, J.; Infante, I.C.; Guennou, M.; Adjeroud, N.; Lenoble, D. Mesoporous TiO_2 anatase films for enhanced photocatalytic activity under UV and visible light. *RSC Adv.* **2020**, *10*, 38233–38243. https://doi.org/10.1039/D0RA06455F.
25. Chekir, N.; Benhabiles, O.; Tassalit, D.; Laoufi, N.A.; Bentahar, F. Photocatalytic degradation of methylene blue in aqueous suspensions using TiO_2 and ZnO. *Desalin. Water Treat.* **2016**, *57*, 6141–6147. https://doi.org/10.1080/19443994.2015.1060533.
26. Lee, C.G.; Na, K.H.; Kim, W.T.; Park, D.C.; Yang, W.H.; Choi, W.Y. TiO_2/ZnO nanofibers prepared by electrospinning and their photocatalytic degradation of methylene blue compared with TiO_2 nanofibers. *Appl. Sci.* **2019**, *9*, 3404. https://doi.org/10.3390/app9163404.
27. Kim, W.T.; Na, K.H.; Park, D.C.; Yang, W.H.; Choi, W.Y. Photocatalytic Methylene Blue Degradation of Electrospun Ti–Zn Complex Oxide Nanofibers. *Nanomaterials* **2020**, *10*, 1311. https://doi.org/10.3390/nano10071311.

28. Someswararao, M.V.; Dubey, R.S.; Subbarao, P.S.V. Electrospun composite nanofibers prepared by varying concentrations of TiO_2/ZnO solutions for photocatalytic applications. *J. Photochem. Photobiol. A* **2021**, *6*, 100016. https://doi.org/10.1016/j.jpap.2021.100016.
29. Singh, J.; Kumar, S.; Manna, A.K.; Soni, R.K. Fabrication of ZnO–TiO_2 nanohybrids for rapid sunlight driven photodegradation of textile dyes and antibiotic residue molecules. *Opt. Mater.* **2020**, *107*, 110138. https://doi.org/10.1016/j.optmat.2020.110138.
30. Chen, D.; Zhang, H.; Hu, S.; Li, J. Preparation and enhanced photoelectrochemical performance of coupled bicomponent ZnO−TiO_2 nanocomposites. *J. Phys. Chem.* C **2008**, *112*, 117–122. https://doi.org/10.1021/jp077236a.
31. Liu, X.; Hu, Y.Y.; Chen, R.Y.; Chen, Z.; Han, H.C. Coaxial nanofibers of ZnO-TiO_2 heterojunction with high photocatalytic activity by electrospinning technique. *Synth. React. Inorg. Met.-Org. Nano-Met. Chem.* **2014**, *44*, 449–453. https://doi.org/10.1080/15533174.2013.776590.
32. Kumar, K.; Chitkara, M.; Sandhu, I.S.; Mehta, D.; Kumar, S. Photocatalytic, optical and magnetic properties of Fe-doped ZnO nanoparticles prepared by chemical route. *J. Alloys Compd.* **2014**, *588*, 681–689. https://doi.org/10.1016/j.jallcom.2013.11.127.
33. Habba, Y.G. Capochichi-Gnambodoe, M.; Leprince-Wang, Y. Enhanced photocatalytic activity of iron-doped ZnO nanowires for water purification. *Appl. Sci.* **2017**, *7*, 1185. https://doi.org/10.3390/app7111185.
34. Zhang, Y.; Ram, M.K.; Stefanakos, E.K.; Goswami, D.Y. Enhanced photocatalytic activity of iron doped zinc oxide nanowires for water decontamination. *Surf. Coat. Technol.* **2013**, *217*, 119–123. https://doi.org/10.1016/j.surfcoat.2012.12.001.
35. Wahab, R.; Hwang, I.H.; Kim, Y.S.; Shin, H.S. Photocatalytic activity of zinc oxide micro-flowers synthesized via solution method. *Chem. Eng. J.* **2011**, *168*, 359–366. https://doi.org/10.1016/j.cej.2011.01.038.
36. Triolo, C.; Fazio, E.; Neri, F.; Mezzasalma, A.M.; Trusso, S.; Patanè, S. Correlation between structural and electrical properties of PLD prepared ZnO thin films used as a photodetector material. *Appl. Surf. Sci.* **2015**, *359*, 266–271. https://doi.org/10.1016/j.apsusc.2015.10.120.
37. Santangelo, S. Electrospun nanomaterials for energy applications: Recent advances. *Appl. Sci.* **2019**, *9*, 1049. https://doi.org/10.3390/app9061049.
38. Sekar, A.D.; Manickam, M. Current trends of electrospun nanofibers in water and wastewater treatment. In *Water and Wastewater Treatment Technologies*; Springer: Singapore, 2019; pp. 469–485. https://doi.org/10.1007/978-981-13-3259-3_21.
39. Malara, A.; Frontera, P.; Bonaccorsi, L.; Antonucci, P.L. Hybrid zeolite SAPO-34 fibres made by electrospinning. *Materials* **2018**, *11*, 2555. https://doi.org/10.3390/ma11122555.
40. Busacca, C.; Donato, A.; Faro, M.L.; Malara, A.; Neri, G.; Trocino, S. CO gas sensing performance of electrospun Co_3O_4 nanostructures at low operating temperature. *Sens. Actuators B Chem.* **2020**, *303*, 127193. https://doi.org/10.1016/j.snb.2019.127193.
41. Sun, Y.; Cheng, S.; Lu, W.; Wang, Y.; Zhang, P.; Yao, Q. Electrospun fibers and their application in drug controlled release, biological dressings, tissue repair, and enzyme immobilization. *RSC Adv.* **2019**, *9*, 25712–25729. https://doi.org/10.1039/C9RA05012D.
42. Zhang, X.; Shi, X.; Gautrot, J.E.; Peijs, T. Nanoengineered electrospun fibers and their biomedical applications: A review. *Nanocomposites* **2021**, *7*, 1–34. https://doi.org/10.1080/20550324.2020.1857121.
43. Folino, A.; Triolo, C.; Petrovičová, B.; Pantò, F.; Zema, D.A.; Santangelo, S. Evaluation of Electrospun Self-Supporting Paper-Like Fibrous Membranes as Oil Sorbents. *Membranes* **2021**, *11*, 515. https://doi.org/10.3390/membranes11070515.
44. Ponti, A.; Raza, M.H.; Pantò, F.; Ferretti, A.M.; Triolo, C.; Patane, S.; Pinna, N.; Santangelo, S. Structure, Defects, and Magnetism of Electrospun Hematite Nanofibers Silica-Coated by Atomic Layer Deposition. *Langmuir* **2020**, *36*, 1305–1319. https://doi.org/10.1021/acs.langmuir.9b03587.
45. Rafidah, J.; Mohd-Sahaid, K.; Norliza, A.R.; Aidil, A.H.; Mohd-Farid, A. Effect of sodium hydroxide pretreatment on chemical composition of treated acacia mangium using response surface methodology. *J. Trop. For. Sci.* **2020**, *32*, 391–401. https://doi.org/10.26525/jtfs2020.32.4.391.
46. Santangelo, S.; Patanè, S.; Frontera, P.; Pantò, F.; Triolo, C.; Stelitano, S.; Antonucci, P. Effect of calcium-and/or aluminum-incorporation on morphological, structural and photoluminescence properties of electro-spun zinc oxide fibers. *Mater. Res. Bull.* **2017**, *92*, 9–18. https://doi.org/10.1016/j.materresbull.2017.03.062.
47. He, G.; Cai, Y.; Zhao, Y.; Wang, X.; Lai, C.; Xi, M.; Fong, H. Electrospun anatase-phase TiO_2 nanofibers with different morphological structures and specific surface areas. *J. Colloid Interface Sci.* **2013**, *398*, 103–111. https://doi.org/10.1016/j.jcis.2013.02.009.
48. Ranjith, K.S.; Uyar, T. Conscientious design of Zn-S/Ti-N layer by transformation of $ZnTiO_3$ on electrospun $ZnTiO_3$@ TiO_2 nanofibers: Stability and reusable photocatalytic performance under visible irradiation. *ACS Sustain. Chem. Eng.* **2018**, *6*, 12980–12992. https://doi.org/10.1021/acssuschemeng.8b02455.
49. Mebrek, A.; Alleg, S.; Benayache, S.; Benabdeslem, M. Preparation and characterization of spinel type Zn_2TiO_4 nanocomposite. *Ceram. Int.* **2018**, *44*, 10921–10928. https://doi.org/10.1016/j.ceramint.2018.03.153.
50. Arin, J.; Thongtem, S.; Phuruangrat, A.; Thongtem, T. Template synthesis of Zn_2TiO_4 and $Zn_2Ti_3O_8$ nanorods by hydrothermal-calcination combined processes. *Mater. Lett.* **2017**, *193*, 270–273. https://doi.org/10.1016/j.matlet.2017.01.142.
51. Kanjwal, M.A.; Sheikh, F.A.; Barakat, N.A.; Li, X.; Kim, H.Y.; Chronakis, I.S. Zinc oxide's hierarchical nanostructure and its photocatalytic properties. *Appl. Surf. Sci.* **2012**, *258*, 3695–3702. https://doi.org/10.1016/j.apsusc.2011.12.008.
52. Otieno, F.; Airo, M.; Erasmus, R.M.; Billing, D.G.; Quandt, A.; Wamwangi, D. Structural and spectroscopic analysis of ex-situ annealed RF sputtered aluminium doped zinc oxide thin films. *J. Appl. Phys.* **2017**, *122*, 075303, https://doi.org/10.1063/1.4998939.

53. Ohsaka, T.; Izumi, F.; Fujiki, Y. Raman spectrum of anatase, TiO_2. *J. Raman Spectrosc.* **1978**, *7*, 321–324. https://doi.org/10.1002/jrs.1250070606.
54. Du, Y.L.; Deng, Y.; Zhang, M.S. Variable-temperature Raman scattering study on anatase titanium dioxide nanocrystals. *J. Phys. Chem. Solids* **2006**, *67*, 2405–2408. https://doi.org/10.1016/j.jpcs.2006.06.020.
55. Arin, J.; Thongtem, S.; Phuruangrat, A.; Thongtem, T. Characterization of ZnO–TiO_2 and zinc titanate nanoparticles synthesized by hydrothermal process. *Rev. Chem. Intermed.* **2017**, *43*, 3183–3195. https://doi.org/10.1007/s11164-016-2818-y.
56. Sáenz-Trevizo, A.; Pizá-Ruiz, P.; Chávez-Flores, D.; Ogaz-Parada, J.; Amézaga-Madrid, P.; Vega-Ríos, A.; Miki-Yoshida, M. On the discoloration of methylene blue by visible light. *J. Fluoresc.* **2019**, *29*, 15–25. https://doi.org/10.1007/s10895-018-2304-6.
57. Mohamadi Zalani, N.; Koozegar Kaleji, B.; Mazinani, B. Synthesis and characterisation of the mesoporous ZnO-TiO_2 nanocomposite; Taguchi optimisation and photocatalytic methylene blue degradation under visible light. *Mater. Technol.* **2020**, *35*, 281–289. https://doi.org/10.1080/10667857.2019.1678087.
58. Choudhury, B.; Bayan, S.; Choudhury, A.; Chakraborty, P. Narrowing of band gap and effective charge carrier separation in oxygen deficient TiO_2 nanotubes with improved visible light photocatalytic activity. *J. Colloid Interface Sci.* **2016**, *465*, 1–10. https://doi.org/10.1016/j.jcis.2015.11.050.
59. Montenegro, D.N.; Hortelano, V.; Martínez, O.; Martínez-Tomas, M.C.; Sallet, V.; Muñoz-Sanjosé, V.; Jiménez, J. Non-radiative recombination centres in catalyst-free ZnO nanorods grown by atmospheric-metal organic chemical vapour deposition. *J. Phys. D Appl. Phys.* **2013**, *46*, 235302. https://doi.org/10.1088/0022-3727/46/23/235302.
60. Sarkar, K.; Braden, E.V.; Fröschl, T.; Hüsing, N.; Müller-Buschbaum, P. Spray-deposited zinc titanate films obtained via sol–gel synthesis for application in dye-sensitized solar cells. *J. Mater. Chem. A* **2014**, *2*, 15008–15014. https://doi.org/10.1039/C4TA02031F.
61. Mekasuwandumrong, O.; Pawinrat, P.; Praserthdam, P.; Panpranot, J. Effects of Synthesis Conditions and Annealing Post-Treatment on the Photocatalytic Activities of ZnO Nanoparticles in the Degradation of Methylene Blue Dye. *Chem. Eng. J.* **2010**, *164*, 77–84. https://doi.org/10.1016/j.cej.2010.08.027.
62. Al-Shamali, S.S. Photocatalytic degradation of methylene blue in the presence of TiO_2 catalyst assisted solar radiation. *Aust. J. Basic Appl. Sci.* **2013**, *7*, 172–176.
63. Ali, A.S.; Khan, I.; Zhang, B.; Nomura, K.; Homonnay, Z.; Kuzmann, E.; Kubuki, S. Photo-Fenton degradation of methylene blue using hematite-enriched slag under visible light. *J. Radioanal. Nucl. Chem.* **2020**, *325*, 537–549. https://doi.org/10.1007/s10967-020-07238-x.
64. Le, T.K.; Flahaut, D.; Martinez, D.D.; Nguyen, H.K.H.; Huynh, T.K.X. Study of the effects of surface modification by thermal shock method on photocatalytic activity of TiO_2 P25. *Appl. Catal. B. Environ.* **2015**, *165*, 260–268. https://doi.org/10.1016/j.apcatb.2014.10.024.
65. Lee, C.G.; Javed, H.; Zhang, D.; Kim, J.H.; Westerhoff, P.; Li, Q.; Alvarez, P.J.J. Porous Electrospun Fibers Embedding TiO_2 for Adsorption and Photocatalytic Degradation of Water Pollutants. *Environ. Sci. Technol.* **2018**, *52*, 4285–4293. https://doi.org/10.1021/acs.est.7b06508.
66. Fan, G.; Zhan, J.; Luo, J.; Zhang, J.; Chen, Z.; You, Y. Photocatalytic degradation of naproxen by a H_2O_2-modified titanate nanomaterial under visible light irradiation. *Catal. Sci. Technol.* **2019**, *9*, 4614–4628. https://doi.org/10.1039/C9CY00965E.
67. Zhu, K.R.; Zhang, M.S.; Chen, Q.; Yin, Z. Size and phonon-confinement effects on low-frequency Raman mode of anatase TiO_2 nanocrystal. *Phys. Lett. A* **2005**, *340*, 220–227. https://doi.org/10.1016/j.physleta.2005.04.008.
68. Balaji, S.Y.D.J.R.; Djaoued, Y.; Robichaud, J. Phonon confinement studies in nanocrystalline anatase-TiO_2 thin films by micro Raman spectroscopy. *J. Raman Spectrosc.* **2006**, *37*, 1416–1422. https://doi.org/10.1002/jrs.1566.
69. Naldoni, A.; Allieta, M.; Santangelo, S.; Marelli, M. Fabbri, F.; Cappelli, S.; Dal Santo, V. Effect of nature and location of defects on bandgap narrowing in black TiO_2 nanoparticles. *J. Am. Chem. Soc.* **2012**, *134*, 7600–7603. https://doi.org/10.1021/ja3012676.
70. Ai, L.; Zhang, C.; Liao, F.; Wang, Y.; Li, M.; Meng, L., Jiang, J. Removal of methylene blue from aqueous solution with magnetite loaded multi-wall carbon nanotube: Kinetic, isotherm and mechanism analysis. *J. Hazard. Mater.* **2011**, *198*, 282–290. https://doi.org/10.1016/j.jhazmat.2011.10.041.
71. Ani, I.J.; Akpan, U.G.; Olutoye, M.A.; Hameed, B.H. Photocatalytic degradation of pollutants in petroleum refinery wastewater by TiO_2-and ZnO-based photocatalysts: Recent development. *J. Clean. Prod.* **2018**, *205*, 930–954. https://doi.org/10.1016/j.jclepro.2018.08.189.